Microstructural study of micron-sized craters simulating Stardust impacts in Aluminium 1100 targets

Hugues LEROUX [1] Janet BORG[2], David TROADEC[3], Zahia DJOUADI[2], Friedrich HÖRZ[4],

(1) Laboratoire de Structure et Propriétés de l'Etat Solide - UMR CNRS 8008
Université des Sciences et Technologies de Lille
F-59655 Villeneuve d'Ascq-Cedex France
Hugues.Leroux@univ-lille1.fr

(2) Institut d'Astrophysique Spatiale – UMR CNRS-Université Paris XI 8617
Bâtiment 121, Campus
F-91405 Orsay-Cedex France

(3) Institut d'Electronique de Microélectronique et de Nanotechnologie UMR CNRS 8520
Université des Sciences et Technologies de Lille
F-59655 Villeneuve d'Ascq-Cedex France

(4) NASA Johnson Space Center, ARES, SR Houston, TX 77058, USA

Corresponding author: Hugues Leroux
hugues.leroux@univ-lille1.fr

Submitted to Meteoritics and Planetary Science, October, 31, 2005

Abstract

Various microscopic techniques were used to characterize experimental micro- craters in aluminium foils to prepare for the comprehensive analysis of the cometary and interstellar particle impacts in aluminium foils to be returned by the Stardust mission. First, SEM (Scanning Electron Microscopy) and EDS (Energy Dispersive X-ray Spectroscopy) were used to study the morphology of the impact craters and the bulk composition of the residues left by soda-lime glass impactors. A more detailed structural and compositional study of impactor remnants was then performed using TEM (Transmission Electron Microscopy), EDS, and electron diffraction methods. The TEM samples were prepared by Focussed Ion Beam (FIB) methods. This technique proved to be especially valuable in studying impact crater residues and impact crater morphology. Finally, we also showed that InfraRed microscopy (IR) can be a quick and reliable tool for such investigations. The combination of all of these tools enables a complete microscopic characterization of the craters.

Introduction

Investigation of impact craters produced by hypervelocity particles in various high purity metals has been extensively used 10 - 20 years ago, when collectors were exposed in Low Earth Orbit (LEO) to fluxes of extraterrestrial and man-made grains (e.g., Love et al., 1995). The most outstanding example is the Long Duration Exposure Facility (LDEF) which spent more than 5 years in Space, and which constitutes one of the most reliable sources of information on orbital debris and extraterrestrial grains in LEO (e.g. Hörz et al., 1991; Zolensky et al., 1995; Hörz et al., 2002). The analysis of experimental hypervelocity impacts

produced in light-gas guns by different impactors into both metallic (mainly Al or Au) or composite (like the solar cells) targets was compared to the results obtained in space and emerged in a better understanding of the physics of cratering and the relation between the properties of the impactor (size, density, velocity) and those of the resulting crater (diameter, depth) (Hörz et al., 1994 for metallic targets and Graham et al., 1999a, for craters in solar cells). It appears empirically that the most reliable information on the impacting grains is deduced from the diameter of the craters. In particular, because aluminium is the preferred material for space structures, many impact experiments of soda-lime beads into aluminium were performed, that are described in Bernard and Hörz (1995) or Hörz et al. (1995).

Although a considerable amount of information was obtained by using metallic targets for the collection of extraterrestrial grains, such targets were not so much favoured in recent years, following the development of targets with low densities that allow for the soft capture of the same particles in an unmolten, more or less “intact” manner. Among those low density targets, SiO_2-based aerogel is now commonly used in space for collecting particles, most recently for the Orbital Debris Collection Experiment (ODCE) (Hörz et al., 2000) and as the collector surface of the Stardust mission (Brownlee et al., 2003).

The primary goal of the various analyses contemplated for the craters resulting from cometary and interstellar grain collisions on the Stardust spacecraft is to provide as much information as possible on the fluence, size distribution and general composition of the impactors. Although it is expected that the most detailed information will be obtained from the analyses of the grains captured in aerogel, Stardust also exposed Al foils that were used to hold the aerogel samples in their modular trays; investigation of these foils will yield complementary information to the aerogel collectors, predominantly size distribution and particle fluxes. Indeed, crater-morphology and size is more readily converted into initial impactor size than the morphology and size of aerogel penetration tracks, the latter strongly

depending on potential projectile fragmentation and complex processes during projectile deceleration (Anderson and Ahrens, 1994).

The analytical procedures used to characterize small impact craters underwent considerable development and improvement in recent years and the potential exists to deduce much more about the impactors, now compared to 10-15 years ago. The preliminary analyses described here on laboratory craters show the types of information that can currently be derived from careful and systematic analyses of the craters. Such a procedure could be the only reliable way of investigating sub-micron grains of fluffy aggregates that can not be extracted from the aerogel.

In this study we analysed the craters obtained by laboratory impacts of soda-lime beads of various sizes in Al 1100 (~ 99 pure) foils. Such chemically almost pure material is mandatory to obtain good signal-to-noise ratios in the X-ray spectra for the elements that constitute the residue trapped in the crater bottom, walls or rim (except for Al). First, a SEM-FEG investigation was performed, followed by a chemical investigation, using the EDS attached to the instrument. A careful FIB-TEM investigation of a large crater cross section and of two small craters (< 10 μm) was also conducted and demonstrated that the preparation technique by FIB is reliable for the extraction of melted impactor remnants and detailed chemical and isotope analyses. Finally, on some large craters, we showed that a microscopic IR investigation of the crater can lead to quick and reliable information on the incident particle remnants. We shall first briefly describe the samples investigated and the analytical tools before describing our main results. These investigations were complemented by investigations by other members of the Stardust Cratering Preliminary Analysis Team (this MAPS issue). Collectively it is shown that much can be learned about the unknown cometary grains, such as their fluences and size distributions, as well as their bulk and isotopic composition from the investigation of microcraters in aluminium targets. Such analyses are

most likely much easier and quicker than those to be performed on particles trapped in the aerogel collectors, and they are ideally suited for the Preliminary Examination of cometary and interstellar samples to be returned by the Stardust mission.

I. Experimental set-up

We analysed the impact craters in three Al foils from light gas gun experiments #2383, 2388 and 2391 at the NASA Johnson Space Center, Houston. The target foils were flight spares from the Stardust Mission, courtesy of P. Tsou, JPL, and consisted of Al 1100 foils, some 100 μm thick, mounted on a massive Al 6061 plate, the latter simulating the geometry and structure of the Stardust collectors. Soda-lime beads of calibrated sizes were shot-gunned into these targets at a velocity of approximately 6 km/s. More precisely, 50 μm (43-53 μm sieve interval) beads were impacted in sample #2383, 30 μm (20-37 μm sieve interval) beads in #2388 and 15 μm (10-20 μm sieve interval) beads in #2391.

The electron microscopy studies were performed at LSPES (Lille- France). Scanning Electron Microscopy using a Field Emission Gun (SEM-FEG) was accomplished on a SEM-FEG Hitachi S4700. All images were recorded in Secondary Electron (SE) mode, using the two SE detectors. The lower SE detector is located inside the specimen chamber while the upper SE detector is located inside the lens (*in lens* detector), and allows high resolution images. Usually we used an acceleration voltage of 5 kV for the lower detector and 20 kV for the upper detector, and a working distance of about 10-12 mm. We took pictures of all large craters, generally corresponding to the nominal impactor(s). We also analysed some of the numerous small craters present on sample #2391 that may be attributed to either gun debris, predominantly abrasion product from the gunbarrel and thus stainless steel, or small fragments of larger soda-lime beads; some of the nominal impactors may disintegrate during gun acceleration, because they contain flaws (bubbles; microcracks etc). On sample #2388,

we performed a crater cross section that was studied by SEM-EDS. Chemical analyses were performed with the Energy Dispersive Spectroscope (EDS) system available on the microscope (Noran – Voyager), recorded either as spectra of select regions of interest, or as elemental maps of major elements.

We used a FIB to make cross sections of craters, and to prepare TEM specimens, also at Lille (IEMN), using a Dual Beam FEI Strata DB235 workstation. TEM specimens of two "small" craters of #2391 and of a large crater cross section of #2388 were prepared. Dual beam technique allows sample preparation and compositional observations simultaneously. The electron beam consists of a field emission source and the ion beam consists of a liquid/metal gallium source. The microscope is equipped with a Scanning Transmission Electron Microscope (STEM) detector. The transfer of the electron transparent section to a TEM grid support ("lift out") is performed outside the microscope using a micromanipulator. TEM work was done at Lille (LSPES) on a FEI Tecnai G2 20 microscope, operating at 200 kV (LaB6 filament). The microstructure was studied by direct TEM imaging (bright and dark field modes) or in the STEM mode (bright and dark fields), associated with the corresponding Selected Area Electron Diffraction (SAED) patterns. The micro-chemical analyses were obtained with the Energy Dispersive System (EDS) attached to the TEM (Si diode – EDAX).

Finally, IR-microscopy analyses were performed on a few #2388 craters at IAS (Orsay, France). We used Fourier Transform InfraRed (FTIR) spectroscopy, with a Nicolet Magna-IR ESP spectrometer attached to a Nicolet Nicplan IR microscope, equipped with a Schwarzchild Cassegrain objective (32x) and a condenser (10x), and used in the reflection mode. A variable diaphragm allows to vary the analytical window between 15 and 100 μm on the sample. The spectrometer is equipped with a standard light source (Globar), a KBr beamsplitter, and a nitrogen cooled Mercury-Cadmium-Tellure (MCT) detector working in

the 4000 to 650 cm^{-1} region. The diagnostic signature of the soda-lime glass remnants resides in the 1000 cm^{-1} region.

II. SEM-EDS results

1. Size-frequency distribution of impact craters

A crucial aspect of the impact crater investigation of the Stardust aluminium foils is the correlation between the size of the crater and the size of the incident particle at any given velocity (e.g. Hörz et al. 1995 for Al1100). This correlation is typically given as the ratio of Dc/Dp, where Dc is the crater diameter and Dp the diameter of the incident particle. The velocity of the present impact experiments and the encounter velocity of the Stardust particles are roughly the same, around 6 km/s, by design. The experimental correlation factor is thus directly applicable to the Stardust surfaces.

Table 1 gives our measurements of crater sizes. Dc refers to rim-crest-to-rim-crest dimensions; 3 or 4 diameter measurements were performed and averaged for any specific event, especially for the case of non spherical craters, as described in Murr et al. (1998). Figure 1 shows the procedure used on a large crater of sample #2388. Our measurements give a mean Dc/Dp ratio of ~ 4.3, averaged for the three size distributions (Table 1). This value is modestly smaller than Dc/Dp = 4.63 which was obtained by the dedicated Stardust "calibration" experiments of Kearsley et al. (see companion paper in this issue) that employed more precision sieved glass beads of narrower size intervals. Nevertheless, this shows the great care that will have to be taken in the definition and the measurement of crater diameters. The large size intervals used in the present experiments certainly explain the wide range of crater sizes observed in the case of sample #2391 (see table 1).

In the case of sample #2391, we performed a careful investigation at high magnifications. It appears that the size distribution is dominated by the smaller craters and the

large craters are the minority. We tried to give an estimate of the statistics of small craters; for that, we scanned very carefully a surface of 0,1 cm^2 and observed all craters down to 1 μm in diameter. We found 27 craters (among which 2 of the large ones), with a size distribution centered at about 2-3 μm in diameter. This gives a total of about 500 craters on the whole sample which is 1.3*1.3 cm^2. All are non-ambiguous hypervelocity structures displaying a pronounced, elevated rim. They seem located preferentially around large craters. Most of the unambiguous, small craters are Fe-rich and probably originated from gun debris which are unavoidable for light-gas experiments (e.g., Bernhard and Hörz, 1995). Some of them are Si-rich and would result from the impact of fragmented soda-lime beads. We also detected a very large number of small holes which are not rimmed, typically a few μm in diameter or smaller, that were not counted here.

2. SEM-FEG images of some representative craters

We mainly concentrated on the observation of large craters in the 3 samples analysed, as they are most representative of what is expected in the case of Stardust samples. Figure 2a-b shows a general view at low magnification of craters, as observed in sample #2391. Already at these low magnifications, small craters can be seen. At higher magnifications, many additional small craters are observed, down to sizes of ~ 0.5 μm, below which the surface relief of the aluminium foil does not allow comfortable crater identification.. Fig 3a-b shows two small craters observed in sample #2383.

In order to detail the morphology of the craters, we prepared a half cross section of one crater of sample #2388. Part of the Al-foil containing a big crater has been embedded in epoxy and furthermore progressively eroded until the middle only of the crater remained, that was subsequently polished. Figure 4 shows the half cross section of the crater, as viewed by

SEM. This view confirms that the craters are almost hemi-spherical. All of them have a crest oriented toward the outside of the center, showing target material flow from the inside outward into the rim. These morphologies do not differ significantly from the mm-sized craters previously characterized in comparable target materials, including Al 1100 target foil and soda-lime projectiles (e.g., Murr et al., 1996; Ferreyra et al., 1997). They strongly differ, however, from impacts in solar cell targets where spallation is present, due to brittle target materials (e.g. Graham et al., 1999b and 2001).

The specific morphology of the rims reflects solid-state plastic flow. This flow structure is visible in figure 5 which shows SEM magnification views of the crest of some craters. In the crest, where plastic deformation is high, complex structures are seen. Fractures of the residue layer are pervasive and the residue layer is broken in numerous locations (where pealing is observed), revealing the inside of the aluminium rim (Fig 5b). Melted residues are seen, and they appear like isolated blocks floating on the aluminium crest. Furthermore, most of these fragmented residue layers show brittle behaviour, as revealed by jagged edges, indicating that they were already solidified before the plastic flow regime terminated. On rare occasions one observes evidence for ductile behavior, as illustrated on fig 5c, where we can see filaments joining two parts of residue fragments, filaments due to the fact that the layer was fractured at a temperature above or close to the glass transition temperature.

The inside walls and bottom residue layer present different morphologies. In some craters the residue appears strongly disrupted, with a complex structure of vesicular melt, numerous droplets and presence of ribbon-like melt filaments (Fig. 6a). Such a structure has already been found in many craters from LDEF (e.g., Zolensky et al., 1995) or in experimental soda-lime glass impacts into aluminium (Gwynn et al., 1997). In other craters the residue appears as a continuous undulating and smooth layer (Fig 6b). In all cases, the

residue layer in the crater floor is rather flat and smooth, which suggests a regular thickness. Numerous fractures are present in the residue layer (Fig 6c-d), that probably originated from differential contraction of the silicate layer in contact with aluminium during cooling after the residue layer solidified.

In some craters we also observed some grains of regular shapes which suggest that crystallization of the melt occurred (Fig 7a). When present in the internal wall, the small crystals seem to point in an upward direction (Fig 7b); this probably reveals a memory effect of melt flow along the growing crater walls. Fractures in the residue layer cross-cut the small crystal, indicating that they formed after crystallization (Fig 7c).

The crater cross section of sample #2388 shown in figure 4, as well as its associated EDS element map (in figure 10) and the TEM-FIB results (see section 4.2) confirm that the residue layer is continuous and of constant thickness at the crater bottom; it becomes thinner in the internal walls, and discontinuous near the rim crest (at least for the crater we selected for this cross section). For this crater cross section, the layer thickness is about 1 μm thick at the bottom.

3. EDS chemical analyses.

Table 2 presents the main results for the compositional analyses performed on craters produced by soda-lime glass particles, either as full particles (so-called « large » craters) or as broken pieces (craters for which the Dc/Dp ratio is smaller than 4.3). The compositions are compared to values obtained for mean values of unfired soda-lime glass beads and are given in atomic%; O% has been recalculated assuming a stoichiometric association with cations. Indeed the software quantification process indicated a systematic excess value for oxygen. This apparent excess is well understandable if the residue layer is thinner than the excitation depth of the X-rays. This is clearly the case since the X-rays spectra are always dominated by

aluminium. In table 2 we also give the atomic ratios O/Si, Na/Si and Ca/Si to allow a rapid comparison with the soda-lime glass composition. The elements originally present in the soda-lime particles are present in all spectra, albeit in various proportions with regards to aluminium. These various proportions depend on the thickness of the melted remnants or on specific conditions of analysis (rims near the crest or more close to the bottom). What is systematically observed is a depletion of volatile elements (Na and Mg) relative to the pure soda-lime glass. Enrichment in Fe is also observed, most probably due to the presence of Fe-inclusions in the Al-foil (see results in FIB-TEM, chap.IV) and contamination by tiny Fe particles from the gun. This deviation from the original glass composition shows that the impact melt remnants do not retain the original chemical composition of the target glass composition. For instance, an average of 57 % of Na is lost, relative to Si. Some analyses, that strongly deviate from the average composition, have not been considered in this table.

Table 1 can be complemented by the elemental EDS maps of the major elements, that portray the spatial distribution of these elements in the craters. This has been performed on a few craters, as shown on figures 8 (large crater from sample #2391, rich in soda-lime) and 9 (small crater from sample #2391, rich in Fe) and on the crater cross section described previously (Fig 10). These elemental maps show that there is a very good correlation between the distributions of those elements that originate from the soda-lime beads (O, Si, Na and Ca), thus showing that no location - depended chemical fractionation occurred. In the case of large craters, the remnants of the incident particle are mostly present in the internal wall, while the amount of residue is found to be significantly lower and discontinuous in the lip regions. One also observes on the maps that the remnant elements do not seem to be distributed homogeneously around the crater, but this lack of symmetry is due to the position of the detector and the complex geometry of the crater, and this artefact must not be taken into account. In our X-ray elemental recordings the detector was positioned at the top side of the

maps. For the big craters, the X-rays coming from the floor cannot reach the detector, resulting in a lack of information from such plane view maps. For the small craters, X-rays originating from the crater floor are detected and it appears that most of the melted remnant (Fe-rich or soda-lime-rich) is present in the bottom of the crater but is generally not detectable in the crest.

The EDS mapping performed on the crater cross section (Fig 10) shows that the residue forms an almost continuous layer (about 1 μm in thickness) at the bottom of the crater. Note also that the amount of residue is lower at the crater crest, as already emphazised above. It is possible, from the calculated volume of melted residue, to estimate the fraction of the initial particle that has not been volatilized; this point will be addressed in detail in chapter IV, according to the TEM results which allow a more precise thickness determination.

III. IR micro-spectroscopy results

IR micro spectroscopy is a possible, non-destructive analytical technique, for which no special sample preparation is required. Used in the reflection mode, it allows for rapid determination of the presence of particle residue in an impact crater thereby confirming the qualitative conclusions from microscopic observations. The major difficulty is caused by the geometry of the craters, which could be responsible for significant loss. The size of the accessible, analytical window is thus governed by the necessary compromise between the signal loss due to surface roughness and the instrument viewing geometry for the different regions of a given crater (bottom, interior walls and rims).

For the large craters of sample #2388 (the only one analysed here), we used an analytical window of 40*40μm. Note that no such compromise has been identified for small craters with the equipment available in this study; it seems possible to analyze small craters

with a synchrotron incident IR beam, because analytical windows as small as 3*3µm can then be used, with very brilliant sources.

For each crater, we scanned different regions, progressing from the interior of the crater to the external rim. The typical spectra, given in fig. 11, show a significant decrease of the 1000 cm^{-1} band, the signature of the presence of Si-O stretching bonds, from the inside to the outside of the crater, indicating that the residue matter is not uniformly distributed in the crater. This result is in good agreement with the conclusions of the SEM/EDS and FIB-TEM analyses. We did not consider the other features observed in the spectra, most demonstrably due to contamination of the aluminium foil, particularly the features in the region 2800-3000 cm^{-1} that are diagnostic for CH_2 and CH_3 bands,signatures of organic contamination (e.g. by the vaporized projectile sabot made of polyethylene).

In order to compare the original matter of the soda-lime beads with the residue, we analyzed by reflection soda-lime powder dispersed on an Al foil; additionally, some crushed beads were sandwiched between two thin films of formvar (a polymer transparent to IR light) for analysis by transmission. The two spectra in fig. 12a and b show the same broad feature in the 1000 cm^{-1} region, but unlike what is observed for the remnant in the craters, no structure can be seen in the 1000 cm^{-1} band, consistent with the amorphous nature of the glass samples. The double structure of the band inside the crater is interpreted to reflect incipient crystallization of the soda-lime glass melt, consistent with the SEM imagery of crystal growth in some craters (see figures 7a and b). This crystallization could be due to the annealing of the material during the impact; the evolution of the 1000 cm^{-1} band of silicates during annealing at elevated temperatures has been described by Djouadi et al. (2005).

IV. FIB-TEM exploration

1. Small craters (Si-rich and Fe-rich)

FIB-TEM studies were performed on two small craters with diameters around 10 μm. After being selected by SEM imaging and EDS, each crater was completely recovered by platinum (including rim and bottom) in the FIB workstation. The Pt layer is used to protect the sample from excessive ion etching in the area of interest. During nano-machining, we used a beam current ranging from 20 nA (initial excavation) to 50 pA (final polishing). Figures 13a-c show a half section of such a small crater performed with the FIB dual beam workstation. FIB work allows for imaging of impact feature in 3D, and thus for an accurate determination of thickness and spatial distribution of projectile residues. This cross sectioning reveals that the crater is lined by a continuous thin melt layer, well visible on figure 13c between the Pt coating and the aluminium substrate foil. For the TEM work, two small craters were selected, one rich in Fe and one due to a small soda-lime glass fragment (called Si-rich crater in the following). Figure 14a shows a crater (Si-rich) during the FIB preparation, before final thinning to a thickness of 100 nm. This preparation technique allows the entire crater to be transparent to the TEM electron beam, as shown on figure 14b.

The TEM and STEM studies reveal that the aluminium in not strongly deformed, in contrast to the mm-sized craters formed in face-centered cubic metals or alloys (e.g., Murr et al., 1997, Ferreyra et al., 1997; Murr et al., 1998). In such mm-sized craters, hypervelocity impact cratering induces in metals (for both bcc and fcc cubic structures) a wide, annular region of plastic deformation, extending from the crater walls in the form of dislocation cells or dislocation microbands. In the small craters that we studied, the dislocation density does not appear strongly increased in the aluminium close to the crater bottom or walls. For these small craters (10 μm diameter), the shock pressure probably decreased very rapidly compared to typical dimensions of the component Al-crystals. In areas corresponding to the craters lips, we observed the formation of elongated dislocation cells (Fig. 15a). Recrystallization is observed in areas very close to the crater walls (Fig. 15b) on an almost continuous layer about

500 nm thick. These small new grains (200-300 nm in diameter) probably originate from dynamic recrystallization, as commonly observed in mm-sized craters between the crater walls and the plastically deformed materials (e.g., Murr et al., 1997; Ferreyra et al., 1997; Murr et al., 1998).

Projectile residue is found in the form of a thin layer in contact with the crater walls. In case of the small Fe-rich crater, the layer consists of a polycrystalline iron, with grain sizes of typically 30 nm in diameter (Fig 15c). EDS spectra show that some Al is also present (about 20 %), suggesting mixing between the Fe impactor and the aluminium target. In case of the small Si-rich crater, the residue layer is also found to be nearly continuous with a thickness ranging from 20 to 100 nm, and consisting of an amorphous material. The EDS spectra indicate the presence of Si, O (major elements), as well as Ca, Mg, Na and Al (minor elements). The Al-content is very low, suggesting that mixing of the silicate impactor with the metallic Al-target was absent or very limited, especially if some of the detected Al would derive from the actual Al-substrate. Sodium is found to be strongly depleted. A substantial fraction of sodium has been volatilized during the impact, as already mentioned from EDS results on the SEM. Electron irradiation during TEM-EDS analysis could also favour Na loss. Despite these complexities, it is clear that this crater originated from a soda-lime projectile.

2. Large crater

FIB-TEM work has been performed on a large crater of sample #2388. For that we used the crater cross section already shown in figure 4, with its associated elemental map shown on figure 10. Two TEM foils were extracted, one at the bottom and the other in the upper internal wall, near the crest. Figure 16a shows the location of TEM foil extraction in the FIB workstation. Figure 16b shows the same cross section, with the sample rotated through an

angle of about 45° within the FIB dual beam workstation, after the extraction of the first TEM foil (near the crest).

Figure 17a shows a part of the TEM foil prepared by FIB that was dislodged from the crater floor. The residue layer is thick (1.2 μm) and continuous. This configuration allows for easy measurement of its composition, which is found in good agreement with the SEM – EDS results. Volatile elements such as Na and Mg are found strongly depleted compared to the initial soda-lime composition. Oxygen is also found depleted but its variation has not been measured because the sample thickness is not known with enough precision. All these results are in very good agreement with the SEM-EDS observations. The residue layer contains some radial fractures which are probably related to the fractures observed by SEM in the crater floor (shown on fig. 6d). The recrystallized area in aluminium is much more extended (average thickness of about 5 μm) than for the small craters. The grain size is also found larger (typically 0.5 μm). In contact with this recrystallized area, the aluminium is plastically deformed but the dislocation density is not high. Dislocations are organized into sub-grain boundaries (Fig. 17c).

Figure 18a shows the entire TEM foil prepared by FIB that was taken from the crater wall, near the crest. The residue layer is found to be thinner and discontinuous. Its maximum thickness is 0.4 μm; its composition does not differ from the layer at the crater floor. Locally some irregular vugs are present at the interface with aluminium (Fig. 18b). The low residue thickness, compared to that of the crater floor, is probably explained by an increase in plastic flow in these areas during the formation of the crest. During the plastic flow, the residue layer is stretched, thus its thickness is being decreased, and possibly fractured if the viscosity of this layer is becoming too high. Recrystallized aluminium is also present in contact with the residue layer, but it is thinner (typically 2 μm) than on the crater floor. Beyond this recrystallized zone, the aluminium is found intensely deformed as illustrated by the high

dislocation density. Figure 18c shows a typical dislocation microstructure observed in the plastically deformed area.

The observed distribution of residue within the crater allows an estimate of the total residue volume. If we assume a homogeneous thickness of 1 μm (this value is probably overestimated) and a hemi-spherical geometry, the volume of the residue is close to 1.4×10^3 μm^3. For sample #2388, the nominal radius of the soda-lime impactor was 15 μm and its associate volume is 1.3×10^4 μm^3. This calculation shows that less than 10 % of the impactor was trapped within the crater. The soda-lime glass impactor has either been almost fully volatilised or it was largely ejected beyond the crater rim.

Conclusions

The combination of both detailed microscopic and spectroscopic investigations provides for complementary information and characterization of impact features under conditions that are similar to what is expected in the comet Wild-2 environment. The encounter velocity of Wild-2 dust and the Stardust Al-foils is practically the same (around 6 km/s) as in these laboratory experiments. EDS microanalysis of the aluminium foils demonstrates that the major elements of the impactor residue can be measured reliably and that the initial composition of the impactor can be estimated. However the volatile elements are found to be strongly depleted. IR microspectroscopic analysis proves to be a complementary reliable tool in the characterization of the impactor residue. Our FIB-TEM study demonstrated than less than 10 % of the impactor material is trapped in the crater, all completely melted.

The combined FIB-TEM studies are indicative of the remarkable utility that is afforded by these instruments in the study of impact craters. They allow the full 3D reconstruction of the crater features, including the geometry of the residue layer, and the

internal deformation features in the target. In particular we have shown that the residue layer is thick at the crater floor, and that its thickness becomes progressively thinner in the lateral walls and it is almost absent in the crest. This distribution of remnant material is substantially the result of global plastic flow of the target material during crater formation.

The primary purpose of the cratering studies on the retrieved Stardust Aluminium surfaces will be to obtain the size – frequency distribution of small impact craters and to deduce the associated projectile masses and fluxes, thus complementing the measurements obtained by the active experiments during the flyby of comet Wild-2 (Kissel et al, 2004, Tuzzolino et al, 2004). A secondary objective will be to obtain compositional, possibly isotope information on projectile residues that line the bottoms and walls of these craters. The preliminary investigations performed by the members of the Stardust Cratering Preliminary Examination Team and described in this MAPS issue have clearly shown that these objectives can be reached. In particular, our extended microscopic investigation allows a full description of the impact, both for the target and for the projectile. Of course, great care must be taken when extending our results obtained with large, compact glass beads to what is expected for cometary and interstellar grains, for which the structure is unknown. In particular, our estimation of what impactor fraction (~ 10%) remains inside the crater is difficult to generalize, as it obviously depends on the projectile properties and its ease of shock melting. Highly porous natural aggegates could melt more readily, and thus even less residue is to be found in the craters; on the contrary, projectiles that are dominated by mafic minerals of higher melt temperatures compared to the present soda-lime glass should leave a larger fraction of residue.

Acknowledgements: The authors thank Damien Delattre, Sylvain Denys, Jessy Gillot, Antoine Pagies, Thibault Rudowski and Damien Turckx, all students at the Polytech'Lille,

who helped us to study the craters by SEM, and Guillaume Bouhot, student at Université Paris XI, who helped with the IR analyses. We also thank Jean-François Dhénin for his assistance with TEM. The TEM work was performed at the INSU National Facility for electron microscopy at LSPES, Lille (France). The FIB work was performed through the “plateforme technologique “of IEMN. Financial supports from the CNES (Centre National d’Etude Spatiale) are acknowledged. G. Haynes and T.H. See supported the light gas gun experiments, funded by the Stardust Project, at NASA JSC, Houston.

REFERENCES

Anderson W. and Ahrens T. J. 1994. Physics of interplanetary dust capture via impact into organic foam. *Journal of Geophysical Research E* 99, 2063-2071.

Bernhard R. P. and Hörz F. 1995. Craters in aluminium 1100 by soda-lime glass spheres at 1 to 7 km/s. *International Journal of Impact Engineering* 17:69-80

Brownlee D. E., Tsou T., Anderson J. D., Hanner M. S., Newburn R. L., Sekanina Z., Clark B. C., Hörz F., Zolensky M. E., Kissel J., McDonnell J. A. M., Sandford S. A., Tuzzolino A. J. 2003. *Journal of Geophysical Research* 108, No.E10, 8111, doi:10.1029/2003JE002087

Djouadi Z., d'Hendecourt L., Leroux H., Borg J., Jones A. P., Deboffle D. and Chauvin N. 2005. IR spectroscopic study of silicate recrystallization: first determination of a related activation energy. *Astronomy and Astrophysics* 440:179-185

Ferreyra E., Murr L. E., Garcia E. P., and Hörz F. 1997. Effect of initial microstructure on high velocity and hypervelocity impact cratering and crater-related microstructures in thick copper targets, Part I: Soda-lime glass projectiles. *Journal of Material Science* 32:2573-2585.

Graham G. A., Kearsley A. T., Grady M. M., Wright I. P., Griffiths A. D. and McDonnell J. A. M. 1999a. Hypervelocity impacts in low earth orbit: cosmic dust versus space debris. *Advances in Space Research* 23:95-100

Graham G. A., Kearsley A. T., Grady M. M., Wright I. P., Herbert M. K., and McDonnell J. A. M., 1999b. Natural and simulated hypervelocity impacts into solar cells. *International Journal of Impact Engineering* 23, 319-330.

Graham G. A., McBride N., Kearsley A. T., Drolshagen G., Green S. F., McDonnell J. A. M., Grady M. M. and Wright I. P. 2001. The chemistry of micrometeoroid and space debris

remnants captured on Hubble Space telescope solar cells. *International Journal of Impact Engineering* 26:263-274.

Gwynn D. W., Hörz F., Bernhard R. P. and See T. H. 1997. The dispersion of molten soda-lime glass projectiles following penetration of thin aluminium membranes. *International Journal of Impact Engineering* 20:325-336.

Hörz F., Bernhard R. P., Warren, J. L., See T. H., Brownlee D. E., Laurence M. R., Messenger S. and Peterson R. B. 1991. Preliminary analysis of LDEF instrument AO187-1 "chemistry of micrometeroids experiment". *NASA Conference Publication* 3134 :487–501

Hörz F., Cintala M. J., Bernhard R. P. and See T. H. 1994. Penetration Experiments in aluminium and teflon targets of widely variable thickness. *AIP conference proceedings* 310:329-344

Hörz, F., Bernhard, R.P. and See, T.H. 1995. Hypervelocity Penetration in Aluminium 6061 and 1100 Alloys, in *Shock Wave and High Strain Rate Phenomena, L. E Murr, K. P. Staudhammer, M. A. Meyers, eds.,* Elsevier Science B.V., 1995.

Hörz F., Zolensky M.E., Bernhard R.P. and See T.H. 2000. Impact features and projectile residues in aerogel exposed on Mir. *Icarus* 147:559-579.

Hörz F., Bernhard R. P., See T. H., Kessler D. J. 2002. Metallic and oxidized aluminium debris impacting the trailing edge of the long duration exposure facility (LDEF). *Space Debris* 2:51-66.

Kissel J., Krueger F.R., Silen J. and Clark B.C. 2004 The Cometary and Interstellar Dust Analyzer at Comet 81P/Wild2. *Science* 304, 5678, 1774 – 1776.

Love S.G., Brownlee D.E., King N.L. and Hörz F. 1995. Morphology of meteroid and debris impact craters formed in soft metal targets on the LDEF satellite. *International Journal of Impact Engineering* 16:405-418

Murr L. E., Garcia E. P., Ferreyra E., Niou C. S., Rivas J. M. and Quinones S. A. 1996. Microstructural aspects of hypervelocity impact cratering and jetting in copper. *Journal of Material Science* 31:5915- 5932

Murr L. E., Quinones S. A., Ferreyrat E., Ayala A., Valerio O. L., Hörz F., Bernhard R. P., 1998. The low-velocity-to-hypervelocity penetration transition for impact craters in metal targets. *Materials Science and Engineering A* 256:166-182.

Quinones S. A., Rivas J. M. and Murr L. E. 1995. Deformation and deformation –specific microstructures associated with a hypervelocity impact crater in copper. *Journal of Material Science Letters* 14, 685-688.

Tuzzolino A.J., Economou T.E., Clark B.C., Tsou P., Brownlee D.E., Green S.F., McDonnell J.A.M., McBride N. and Colwell M.T.S.H. 2004 Dust measurements in the coma of comet 81P/Wild2 by the Dust Flux Monitor Instrument. *Science* 304, 5678, 1776 – 1780.

Zolensky M. E., See T. H., Bernhard R. P., Barrett, R., Hörz F., Warren, J. L., Dardano C., Leago K. S., Kessler D. and Foster T. R. 1995. Final activities and results of the long duration exposure facility meteoroid and debris special investigation group. *Advanced Space Research* 16:1153-1165

Table 1

Sample	Soda-lime beads		Large craters size distribution	Mean Dc	Dc/Dp
	Size (μm)	Velocity (km/s)			
#2383	50	6,15	2 large craters Dc = 190/199	195	3,90
#2388	30	6,02	5 large craters Dc = 112/113/123/126/129	120	4,02
#2391	15	6,03	14 large craters Dc = 32/47/57/68/74/75/78/ 81/82/83/83/84/90/93/	73	4,90

Table 1 - Calibration results for the large craters in the three samples #2383, 2388 and 2391, most probably corresponding to the nominal impactor. Note the large discrepancy between the values measured in the case of sample #2391, most probably due to the bead size dispersion.

Table 2

O	Si	Na	Ca	Mg	Fe	O/Si	Na/Si	Ca/si
Soda lime glass								
57.6	22.8	15.2	2.1	2.3	0.1	2.52	0.67	0.09
58.9	24.1	12.2	2.1	2.5	0.1	2.44	0.51	0.09
Craters								
63.1	28.2	3.9	2.1	nd	2.5	2.24	0.14	0.07
61.9	25.9	4.3	4.8	nd	3.1	2.39	0.17	0.19
61.3	26.5	7.7	2.7	0.48	1.2	2.31	0.29	0.10
60.6	24.0	5.5	5.3	0.35	4.1	2.52	0.23	0.22
60.4	25.5	9.4	2.2	0.82	1.7	2.37	0.37	0.09
62.3	27.4	6.1	3.1	-	0.92	2.27	0.22	0.11
62.1	26.2	7.1	1.2	-	3.4	2.37	0.27	0.05
59.5	23.6	12.5	1.3	-	3.2	2.52	0.53	0.06
64.0	28.1	3.7	1.0	-	3.3	2.28	0.13	0.04
62.6	27.0	5.9	1.9	-	2.5	2.32	0.22	0.07
61.9	24.2	6.1	2.6	-	5.3	2.56	0.25	0.11
62.1	24.5	5.4	3.9	-	2.9	2.53	0.22	0.16
64.2	30.0	3.3	2.4	nd	0.06	21.4	0.11	0.08
53.5	9.7	5.3	1.1	nd	30.3	5.51	0.55	0.11
61.8	27.4	7.6	3.2	nd	nd	2.26	0.28	0.12
64.1	29.7	3.1	2.6	nd	0.49	2.16	0.10	0.09
63.4	29.1	4.7	2.0	0.2	0.50	2.18	0.16	0.07
62.2	27.6	6.6	1.7	1.5	0.38	2.25	0.24	0.06
62.8	28.1	5.0	2.4	nd	1.7	2.23	0.18	0.08
60.6	25.6	8.8	1.3	1.5	2.2	2.37	0.34	0.05
57.7	22.2	13.8	3.3	nd	2.9	2.60	0.62	0.15
61.8	26.6	6.2	2.2	nd	3.2	2.32	0.23	0.08
63.7	29.2	3.4	1.6	0.73	1.4	2.18	0.12	0.05
60.5	25.9	9.9	1.5	nd	2.1	2.34	0.38	0.06
62.5	28.2	6.4	1.9	0.83	0.05	2.22	0.23	0.07
58.9	24.8	14.0	1.4	0	0.80	2.37	0.56	0.06
62.8	28.1	5.1	2.3	nd	1.7	2.23	0.18	0.08
62.7	28.7	6.4	1.7	nd	0.32	2.18	0.22	0.06
61.2	26.6	8.5	2.2	1.1	0.41	2.30	0.32	0.08
59.7	23.8	8.5	4.1	1.6	2.1	2.51	0.36	0.17
62.7	28.6	6.2	1.9	nd	0.49	2.19	0.22	0.07

Table 2 : Representative EDS analyses recorded with the SEM (at. %). Oxygen concentration has been recalculated (see text for details). O/Si, Na/Si and Ca/Si atomic ratios are shown for an easy comparison with the mean values measured in soda-lime beads (2,48 for O/Si, 0,59 for Na/Si and 0,09 for Ca/Si)

Figure captions

Figure 1 : SEM image showing a large crater of sample #2388 and the rim-crest to rim-crest method we used for the diameter measurement. The 3 diameters are 126, 128 and 129 μm long, giving a mean value of 127.8 μm.

Figure 2a-b : General views of large craters, originating from sample #2391 and indicative of the systematic presence of small craters surrounding the large ones (SEM in the SE mode with the lower detector).

Figure 3 : SE (upper detector) SEM high magnifications showing two small craters in sample #2383, respectively (a) 8.5 μm and (b) 1.2 μm diameter.

Figure 4 : Half cross section viewed by SEM of a crater from sample 2388

Figure 5 : Magnification views in the crest region of three craters (a) The plastic flow structure oriented toward the crater outside (on the right on the figure) – sample #2388. (b) The residue layer (which appears brighter) is broken at numerous places, particularly where the aluminium crater crest is strongly curved – sample #2391. (c) In some places, the residue layer displays evidence for ductile fractures as shown by the presence of filament joining two broken pieces of residue – sample #2388. All the three figures are SEM images recorded with the upper SE detector.

Figure 6 : SEM images with the upper SE detector (a) Complex structure in a crater interior in sample #2383. The residue consists mostly of ribbon-like melt filaments and droplets (b) The residue appears as a continuous undulating and smooth layer in the internal wall of a crater from sample #2391 (c) Fractures of the residue layer in the crater internal wall, near the crest - sample # 2383 (d) Fractures of the residue layer in the crater bottom of sample #2388. Note that the fractures cut cross some vesicles.

Figure 7 : SEM images with the upper SE detector (a) Crystallites observed in a crater rim of sample #2388. (b) Small crystals observed in the interior of a crater of sample #2388. For this image, the crater was rotated to about 45° in order to better visualize the internal crater wall. Note the upward direction of the crystals. (c) Fractures superimposed on the small crystals, indicative of a fracture event after crystallization.

Figure 8 : X-ray mappings for Al, O, Si and Na performed on a large crater. The lack of symmetry in the element repartition is due to the position of the detector (here at the top side of the maps). The remnants materials seem mainly concentrated in the internal walls of the craters but not in the crests. Note that the detector position does not allow the detection of X-ray coming form the crater floor.

Figure 9 : X-ray maps for Al and Fe corresponding to a small crater, rich in Fe. For these small craters, the topography disruption is lower and the bottom can be mapped in a plane view configuration. The Fe map shows that the residue is mainly in the inside, while the crest is found constituted of Al only.

Figure 10: X-ray maps for Al and Si performed on the crater half cross section shown on figure 4

Fig. 11: IR spectra of 5 different positions (numbered from point 1 to 5) in the same crater. The spectra are relevant to the band evolution from the crater center (point 1) to the external rim (point 5) via the internal “wall” of the crater (point 2), and the external edge (point 4).

Fig. 12: (a) Reflection IR spectrum of some soda-lime beads, crushed and dispersed on an Al foil. This spectrum shows a big structure of amorphous silicates in the region 1000 cm^{-1}, the stretching mode of the Si-O bonds (b) Transmission IR spectrum of some crushed soda lime beads dispersed between two thin films of formvar. It is plotted as absorbance versus wavenumbers. This figure shows a big structure of amorphous silicates in the region 1000 cm^{-1}, the stretching mode of the Si-O bonds.

Fig 13: (a) Small crater selected for FIB nano-machining. The crater is turned at 45° (b) Half crater cross section after FIB work. The interior of the crater was filled with platinum before machining. 3-D morphological features can be reconstructed by recording an image at each step of the erosion process. (c) Magnification showing the interface layer at the bottom edge of the crater, in between platinum and aluminium.

Figure 14: (a) Small crater during FIB machining, before lift out. (b) Entire crater, electron transparent, viewed in the TEM after lift out. This configuration allows a detailed study of the residue layer and deformation features in aluminium. Note the presence of an iron inclusion in the aluminium target.

Figure 15 : TEM results on small craters (a) Si-rich crater - Dislocations cells in an area corresponding to the upper part of the internal wall of the crater, close to the crater lip. Note the presence of the thin, discontinuous, amorphous residue layer. Some decohesion is observed locally at the remnant-aluminium contact (b) Si-rich crater- Recrystallized aluminium in the bottom area of the crater. The recrystallized area do not exceed 500 nm in thickness. The amorphous residue layer appears thicker (100 nm here) and its composition can be measured, as shown by the two contamination spots left after analysis. (c) In the Fe-rich crater, the thin interfacial layer consists of a polycrystalline material (grain size about 30 nm). Note that the residue layer thickness is variable.

Figure 16. (a) Position of the two TEM foils extracted with FIB on the large crater cross section. One foil comes from the crater floor and the other from the internal wall, near the crest (b) Sample after the first extraction (foil near the crest). The sample was rotated by an angle of about 45°. The epoxy-crater interface has been underlined in the bottom of the image to help the morphology recognition of the crater.

Figure 17: TEM micrographs (bright field) from the foil prepared by FIB in the bottom crater (a) General view showing the residue layer in contact with aluminium. Note the fractures in the residue layer, perpendicular to the layer. (b) Recrystallized aluminium in contact with the residue layer. This microstructure originated from dynamical recrystallization during the crater formation. (c) Deeper than the recrystallization layer, the dislocation are organized in subgrain boundaries which evidence an annealing, probably due to the heating event associated to the crater formation.

Figure 18: TEM micrographs (bright field) of the large crater cross-section, from the foil prepared by FIB in internal wall near the crest. (a) General view of the entire TEM foil. Note that the residue layer is thin and discontinuous. Note also than some voids are present locally between aluminium and the remnant material. (b) Magnification showing details of the residue layer and voids at the interface. (c) Deformation microstructure in the aluminium interior. The dislocation density is higher than for the sample coming from the crater bottom.

Microstructural study of micron-sized craters simulating Stardust impacts in Aluminium 1100 targets

By Leroux H., Borg J., Troadec D., Djouadi Z., Hörz F.

Figures

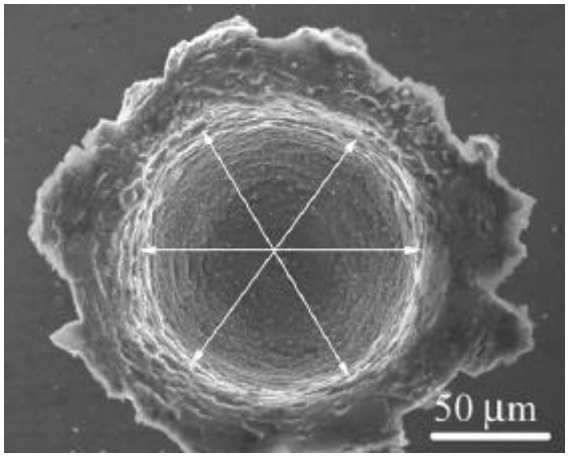

Figure 1

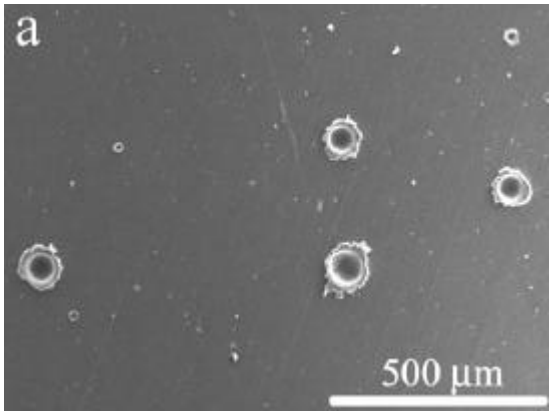

Figure 2a

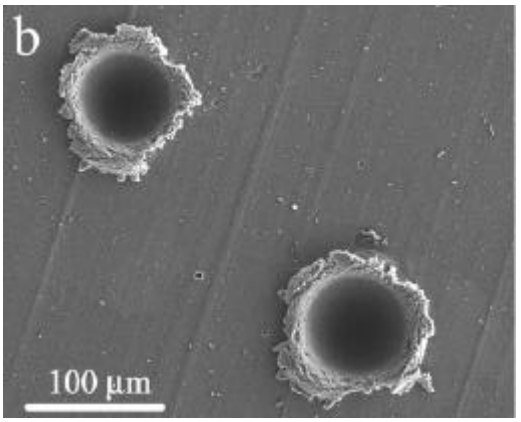

Figure 2b

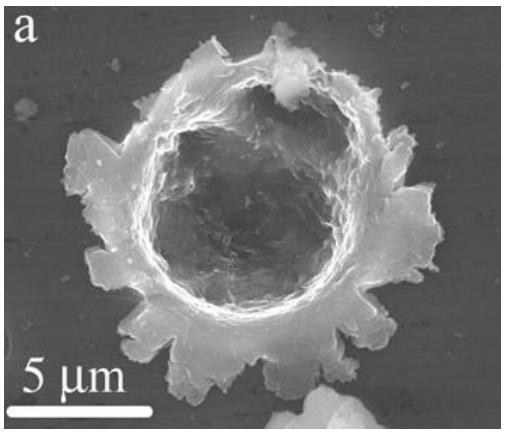

Figure 3a

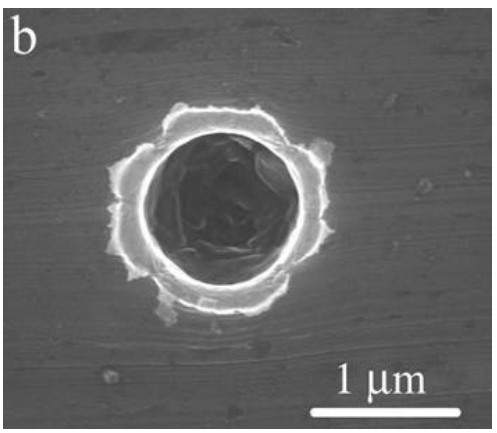

Figure 3b

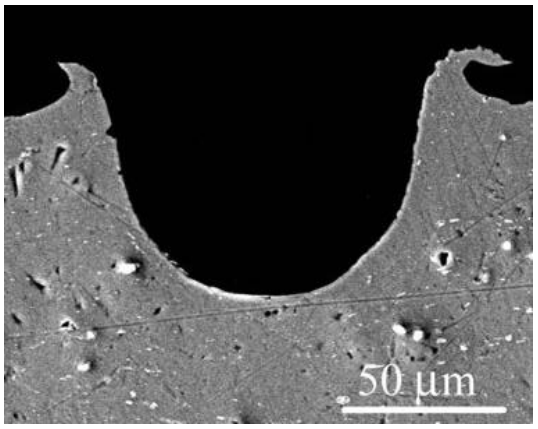

Figure 4

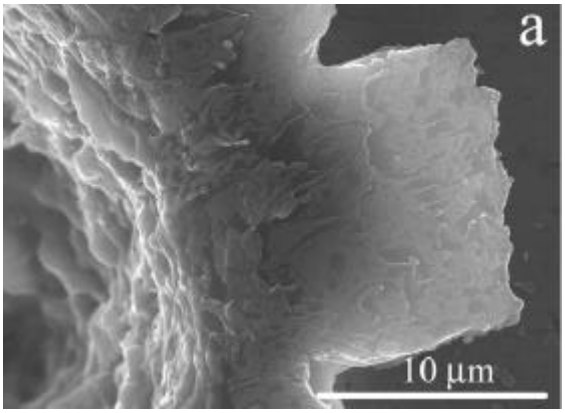

Figure 5a

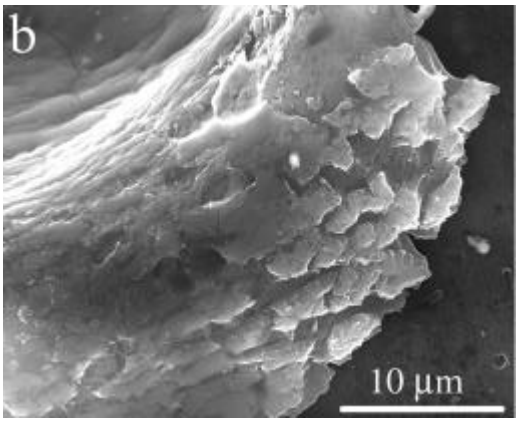

Figure 5b

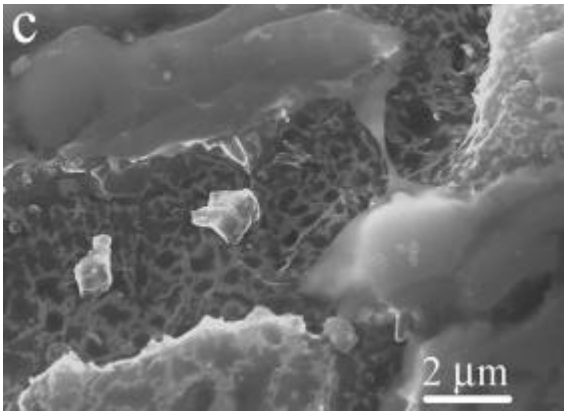

Figure 5c

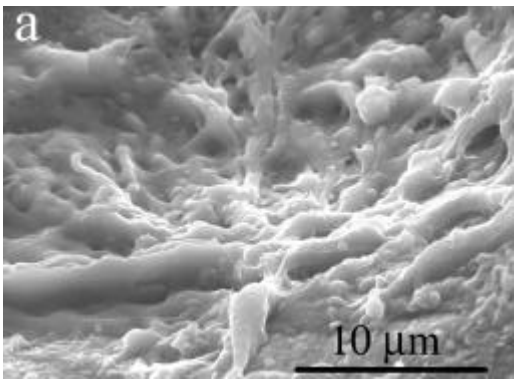

Figure 6a

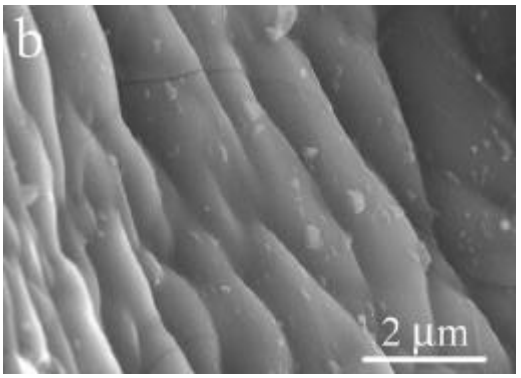

Figure 6b

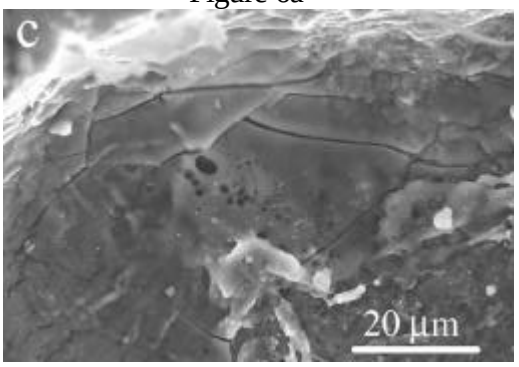

Figure 6c

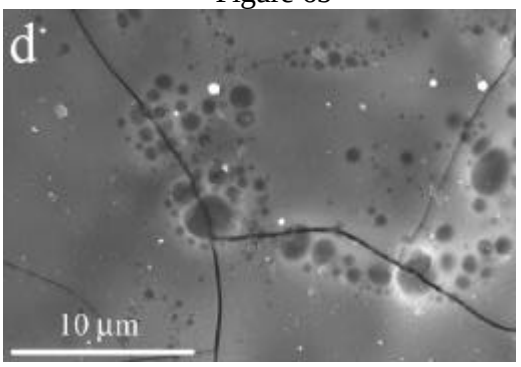

Figure 6d

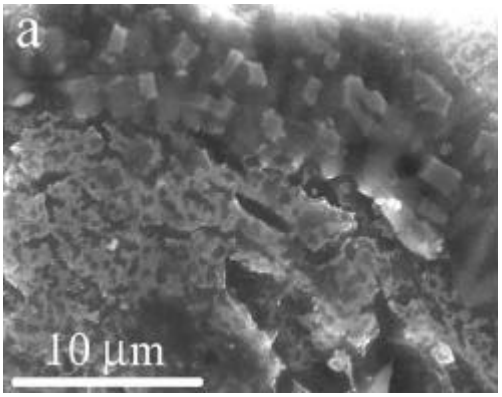

Figure 7a

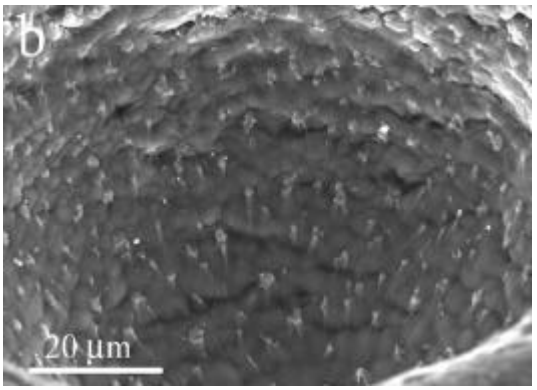

Figure 7b

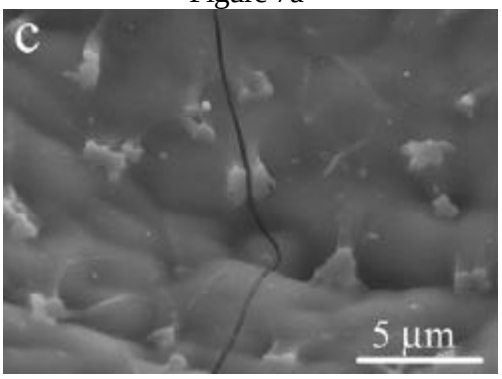

Figure 7c

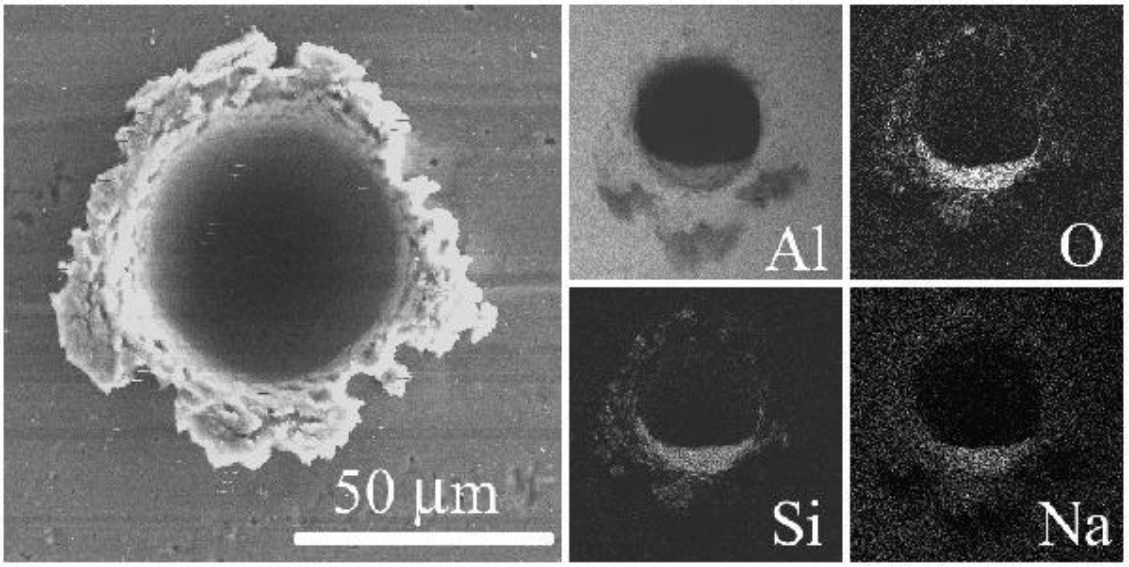

Figure 8

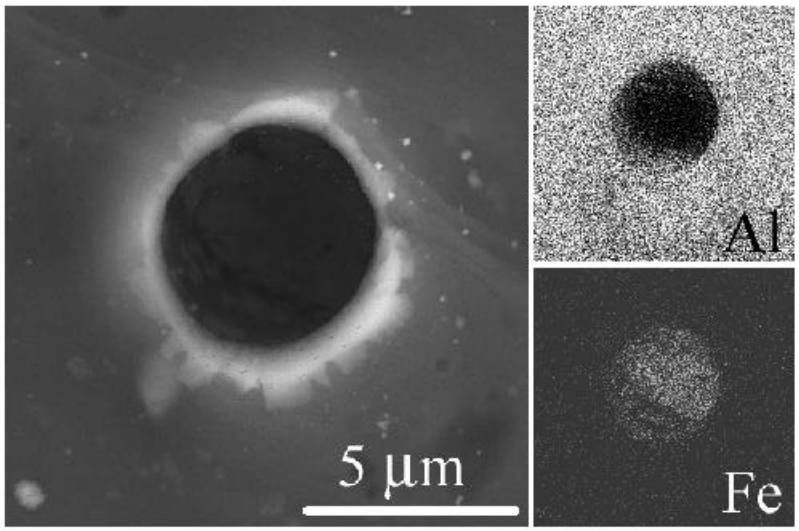

Figure 9

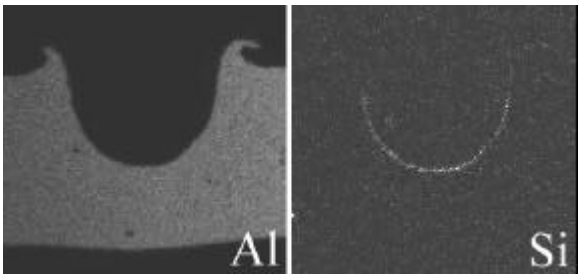

Figure 10

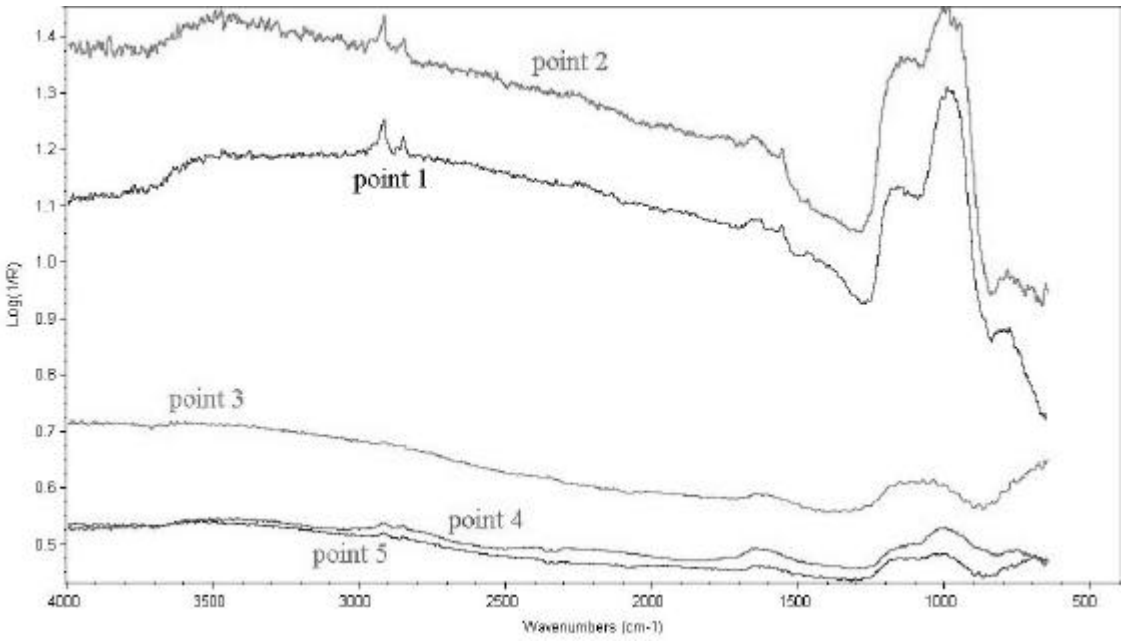

Figure 11

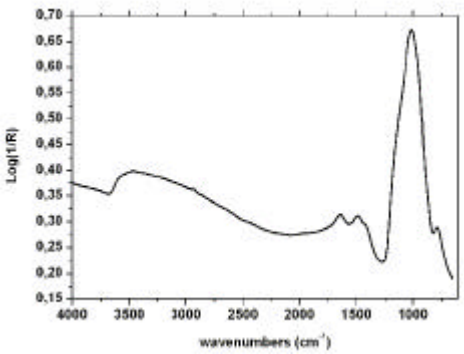

Figure 12a

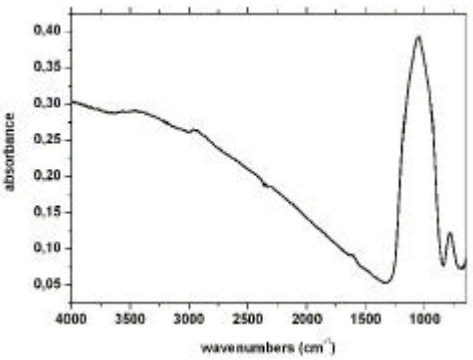

Figure 12b

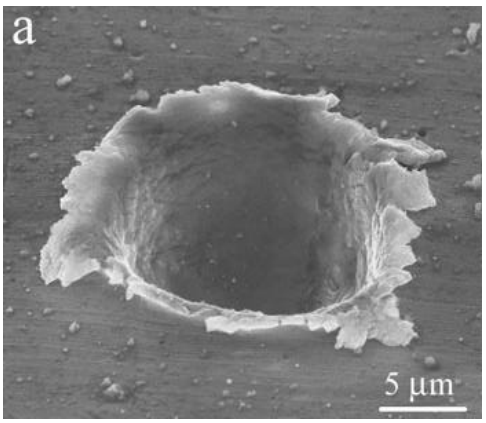

Figure 13a

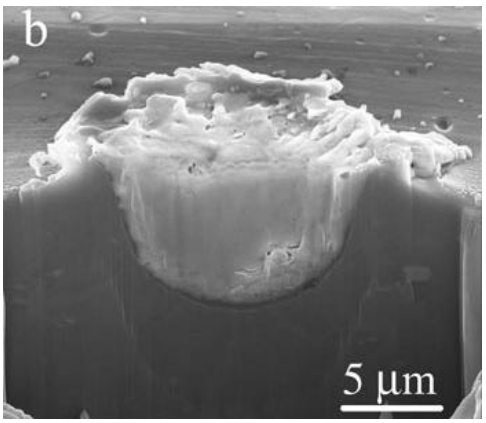

Figure 13b

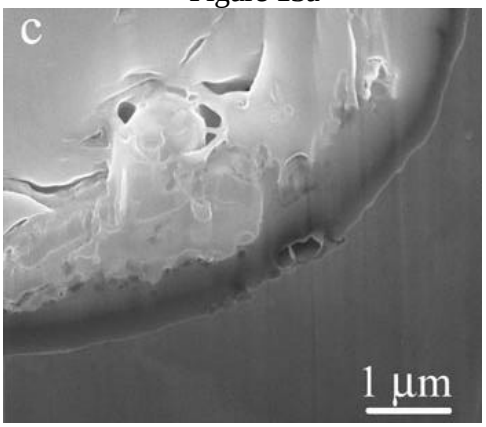

Figure 13a

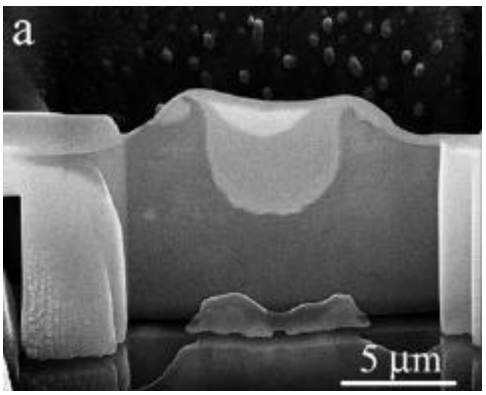

Figure 14a

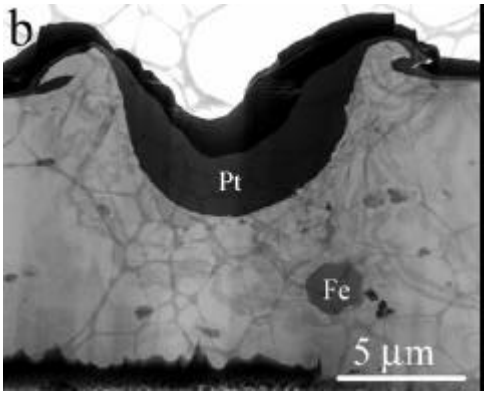

Figure 14b

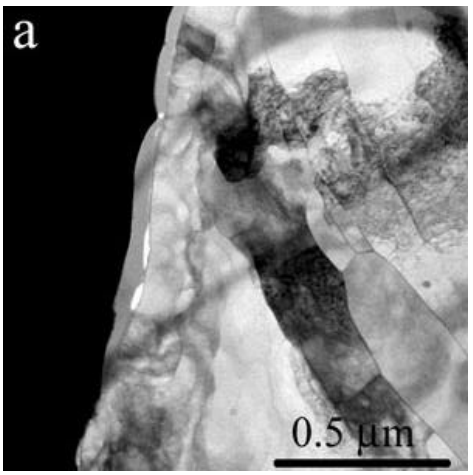

Figure 15a

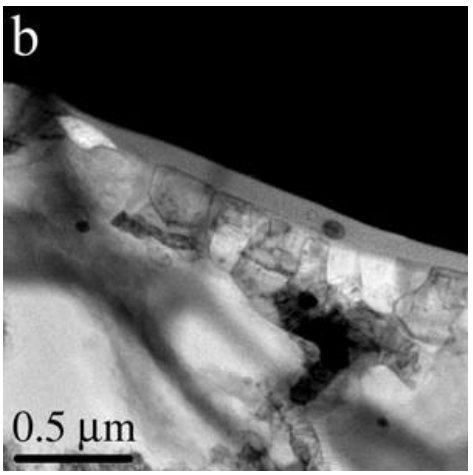

Figure 15b

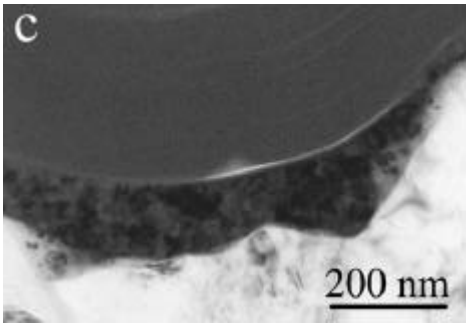

Figure 15c

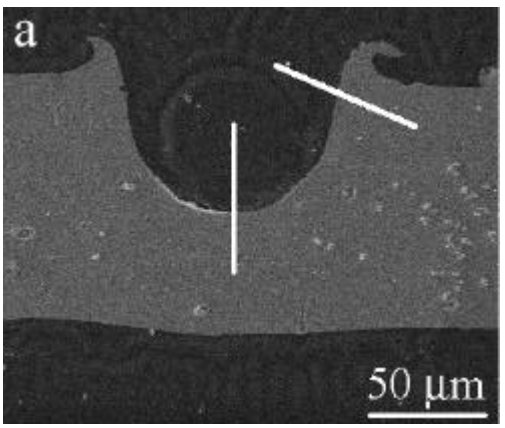

Figure 16a

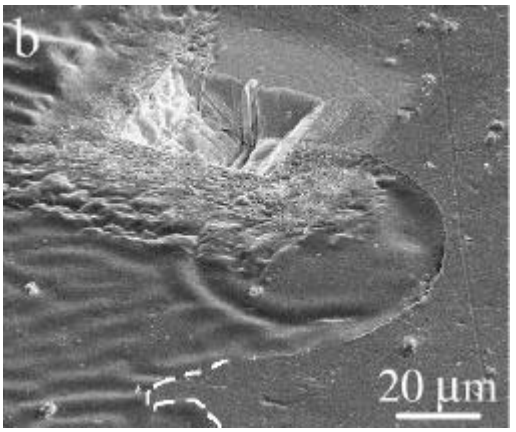

Figure 16b

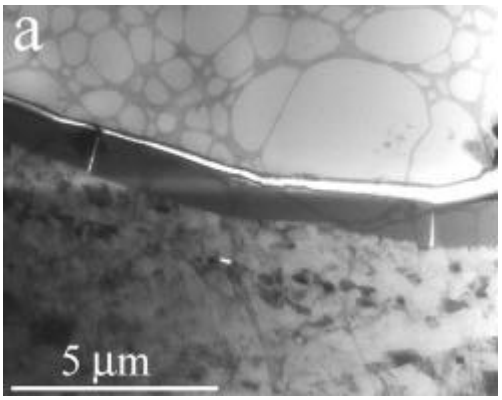

Figure 17a

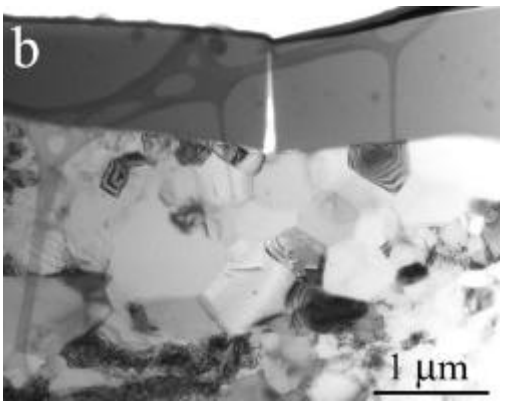

Figure 17b

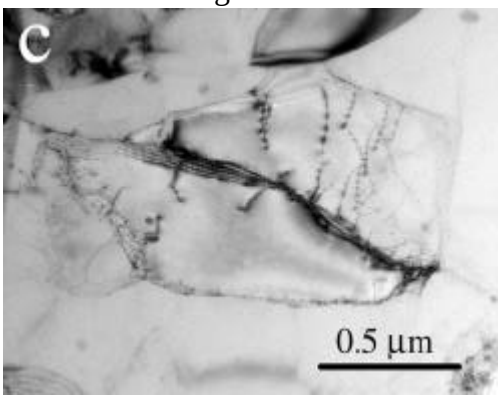

Figure 17c

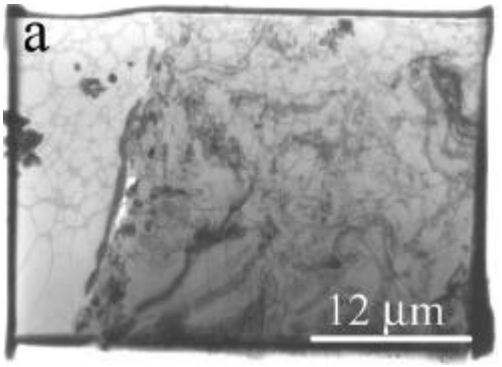

Figure 18a

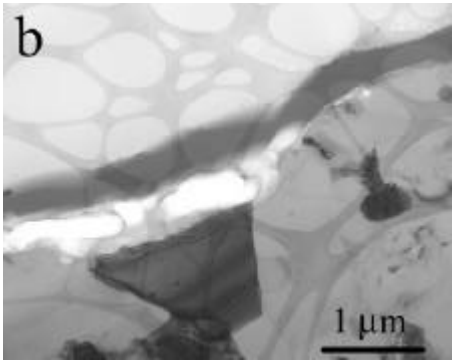

Figure 18b

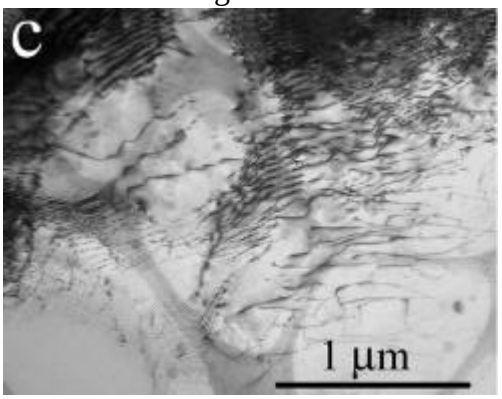

Figure 18c